Renewable Energy 159 (2020) 286–299

Contents lists available at ScienceDirect

Renewable Energy

journal homepage: www.elsevier.com/locate/renene

A shape optimization of ϕ-shape Darrieus wind turbine under a given range of inlet wind speed

Yaoran Chen [a], Jie Su [a], Zhaolong Han [a, b, c, d, *], Yongsheng Zhao [a, b], Dai Zhou [a, b, c, d, **], He Yang [e], Yan Bao [a], Hang Lei [a]

[a] School of Naval Architecture, Ocean and Civil Engineering, Shanghai Jiao Tong University, Shanghai, 200240, PR China
[b] State Key Laboratory of Ocean Engineering, Shanghai Jiao Tong University, Shanghai, 200240, PR China
[c] Key Laboratory of Hydrodynamics of Ministry of Education, Minhang District, Shanghai, 200240, PR China
[d] Shanghai Key Laboratory for Digital Maintenance of Buildings and Infrastructure, Shanghai Jiao Tong University, Shanghai, 200240, PR China
[e] Ocean Engineering Department, Texas A&M University, College Station, TX, 77843, USA

ARTICLE INFO

Article history:
Received 2 December 2019
Received in revised form
30 April 2020
Accepted 9 May 2020
Available online 25 May 2020

Keywords:
ϕ-shape Darrieus turbine
BEM theory
Shape optimization
Inlet wind range
CMAES algorithm
CFD validation

ABSTRACT

The ϕ-shape Darrieus wind turbines have great potential in application due to their omni-directionality and structural advantages. However, to achieve a higher aerodynamic performance, the design of such turbine needs attentive optimization to fit the surrounding wind variation. In this paper, a performance optimization of the shape of ϕ-shape Darrieus wind turbine with a given range of inlet wind speed is carried out. By involving a heuristic search algorithm, Covariance Matrix Adaptation Evolutionary Strategy (CMAES), into Double Multiple Streamtube model (DMST), three geometrical variables of the rotor: the equatorial radius (R), the ratio of radius over half-height (β) and the blade number (B) are modified according to the fitness function that was specially built to satisfy the inlet wind range requirements. Moreover, to validate the optimization output, a 3D CFD simulation is conducted as a comparison. The result shows that this program can present an entirely optimized model under the given range of inlet wind speed, with a 12.5% improved C_p at the optimal velocity compared with the baseline. Verification from CFD method shows a satisfactory agreement for the optimized model compared with the DMST output, indicating that this algorithm could provide a reliable reference for the shape selection of ϕ-shape Darrieus turbines under a certain inlet wind condition.

© 2020 Elsevier Ltd. All rights reserved.

1. Introduction

As a promising candidate for wind harvest, vertical axis wind turbines (VAWTs) have raised increasing interest due to its advantages like simple structure, low noise and omni-directionality [1]. Among various types of VAWTs, the most commonly used type is the Darrieus turbine [2]. Based on the longitudinal section shape of the rotor, Darrieus turbine can be classified into H-shape and ϕ-shape. Out of these, the ϕ-shape turbine can be built with a simpler foundation since it does not need a tower. In addition, the blades of ϕ-rotor are subject to less bending moment than H-rotor because it does not have large centripetal acceleration during rotation. As a result, the ϕ type Darrieus turbine is less fatigable and its lifespan is elongated [3].

Nevertheless, similar to other types of VAWTs, the ϕ-shape Darrieus turbine suffers from low power coefficient. Addressed to this problem, researches have been carried out around the world to improve the performance of VAWTs, both numerically and experimentally. Sandia Laboratory [4,5] conducted their investigations on ϕ type Darrieus turbine by field test and enhanced the power output by changing chord length and the blade-number of the rotor. Singh et al. [6] investigated the influence of the solidity on an H-rotor, concluding that a higher solidity can generally raise the rotor's performance. Li et al. [7] experimentally investigated the effects of pitch angle on the power coefficient, where they found the different optimal pitches for VAWTs with different number of blades. Wang et al. [8] looked into the different thickness and camber configurations for various types of airfoils. Based on their research, modifications on both symmetric and asymmetric NACA

* Corresponding author. School of Naval Architecture, Ocean and Civil Engineering, Shanghai Jiao Tong University, Shanghai, 200240, PR China.
** Corresponding author. School of Naval Architecture, Ocean and Civil Engineering, Shanghai Jiao Tong University, Shanghai, 200240, PR China.
E-mail addresses: han.arkey@sjtu.edu.cn (Z. Han), zhoudai@sjtu.edu.cn (D. Zhou).

https://doi.org/10.1016/j.renene.2020.05.038
0960-1481/© 2020 Elsevier Ltd. All rights reserved.

profiles were suggested to improve the power coefficient. Similar investigations regarding airfoil selection had also been made by Ref. [9]; [10,11] etc.

In recent years, Artificial Intelligence (AI) algorithms have accelerated the process to obtain VAWT with considerably higher aerodynamic performance. Carrigan et al. (2012) [12] used the Differential Evolution (DE) algorithm to demonstrate a totally automatic optimization on the cross-section in two cases of straight-bladed VAWTs, where one of the resultant rotors achieved a power coefficient of 2.4% higher than baseline at TSR = 1. Ma et al. [13] conducted a Multi-Island Genetic Algorithm (MIGA) based optimization on NACA0018 airfoil of a three-blade H-VAWT. The novel profile outperformed at moderate TSRs (less than 1.5) with a maximum growth of 26.82%. Bedon et al. [14–17] optimized the chord length and the thickness of the cross-section of an ϕ type VAWT, where Blade Element Momentum (BEM) theory and Genetic Algorithm (GA) were used. Their resultant design showed uniformly enhancements in low TSR range. Chan and Antar [18,19] independently implemented numerical investigations of parametric sizing optimization on Savonius turbine. Impressively, a maximum improvement of 42.5% at TSR = 0.59 was observed from the research of Antar [19].

However, there is a limitation of researches conducting optimization on the geometrical characteristics of ϕ type rotor, such as: the outline curve and the blade-number. Previous researchers often kept these factors unchanged and focused their investigations on the enhancement of lift and drag coefficients of the profiles. In fact, the influence of the outline shape and the blade-number is not negligible on the rotor performance [20].

On the other hand, most of the above-mentioned literatures carried out the optimization process under a simplex inlet wind speed (which generally is the optimal wind speed from the prototype), and the optimal range for the optimized turbine was unknown before the performance of output would be further tested under different conditions. In another words, there is no guarantee that the design from the optimization process could also be an advanced selection under a pre-desired range of inlet velocities. Such requirement is necessary especially when the region where turbine was placed has a long-term fluctuation of wind speeds.

In order to solve the problem mentioned above, the current work looked into a shape optimization for an ϕ-shape Darrieus turbine, with the object to improve the rotor's power coefficient under a desired range of inlet wind speed.

The Covariance Matrix Adaptation Evolutionary Strategy (CMAES) was invented by Ref. [21]. Among various evolutionary strategies (such as DE, GA etc.), this algorithm shows its great superiority in finding globally optimal solutions and it has been widely validated by former researches under different background scenarios. Rahnamayan et al. [22] compared the convergence speed and the robustness between DE and CMAES algorithms on N-queen problem and concluded the latter one showed a better computational efficiency. Hasenjäger et al. [23] presented an aerodynamic optimization on the shape design of a gas turbine and confirmed the feasibility of CMAES on high-dimensional variables. Athanasiou et al. [24] applied it on the dynamic identification of structural systems under the earthquake and stated that the CMAES algorithm could particularly find exact solutions for a complex sample space than normal evolutionary strategies. Despite these applications in various engineering fields, the use of CMAES in shape optimization of VAWTs was scarce.

Blade Element Momentum theory (BEM) and Computational Fluid Dynamic method (CFD) are two main tools for the aerodynamic analysis of Darrieus turbines. The advantage of BEM based algorithms is their low computational cost, while CFD method has its priority in providing more accurate results. Rossetti et al. [25] investigated the aerodynamic characteristics of a Darrieus turbine using both BEM and 3D CFD methods. He concluded that the CFD analyses could reflect more adequate dynamic effects for low Reynolds number, where conventional BEM method showed remarkable limits. For a large-scaled ϕ-shape Darrieus turbine (Sandia 17m), Delafin et al. [26] adopted the 3D CFD models to implement the analysis and compared it with the results based on BEM algorithm, where the latter method has considerably large computational speed despite the less flow field information. Bedon et al. [14–17] conducted aerodynamic analysis on various types of Darrieus wind turbine using both two methods, suggesting that the CFD method can be a suitable validation for the BEM results. From previous researches, it is believed that the mutual verification of BEM and CFD can make the computation process high-efficient and the results more reliable.

As the main work of this paper, we involved the CMAES algorithm into the Double Multiple Streamtube (DMST) [20] model based on BEM theory. By constructing this framework, we conducted the shape optimization of an ϕ-shape Darrieus turbine for a better outline&blade-number configuration, hoping to achieve higher power coefficients with a given inlet wind range. The contribution of the current work contains following contents: 1. For an ϕ-shape Darrieus wind turbine, a holistic shape optimization, including the outline curve as well as the blade-number, was investigated to achieve a better rotor performance compared with the baseline; 2. At every inlet wind speed within a given range, the power coefficient of the optimized model is improved; 3. On the resultant design from BEM simulation, a 3D CFD simulation was conducted as a supplemented verification.

The whole structure of the current paper is organized as follows. In Section II, the way of turbine modeling, the DMST theory and the CMAES algorithm are presented. In Section III, the optimization results and other outcomes are analyzed and discussed. Validation for the improved model using 3D CFD method is present in Section IV. Finally, essential conclusions from the present work are summarized in Section V.

2. Model and method for optimization

2.1. Modeling of ϕ-shape Darrieus turbine

In this part, the prototype of ϕ-shape Darrieus turbine is modeled and constructed by choosing suitable shape analogue. Parabolic and straight-circular-straight (SCS) curves were formerly adopted as analogies to describe the ideal Troposkien shape of the ϕ-shape Darrieus turbines [4,27,28]. Among these, the parabolic approximation was concluded by Refs. [20] as the most satisfied shape because of the best geometric similarity and the simplicity of modeling (Fig. 1).

Hence, in this paper, the relationship between local radius r and altitude z is described by a quadratic function. Let R denote the equatorial radius and β denote the ratio of radius over half-height. The function can be written as:

$$r = -\frac{\beta^2}{R}z^2 + R \tag{1}$$

Then, the local inclination angle δ can be expressed by the derivative of r at the corresponding local height z:

$$\delta = arctan\left(\frac{2\beta z}{H}\right) \tag{2}$$

Other parameters of the baseline turbine are identical to that of the Sandia 5m [4]. The configurations of Sandia 5m are shown in Table 1, followed by an illustration of the NACA0015 airfoil in Fig. 2:

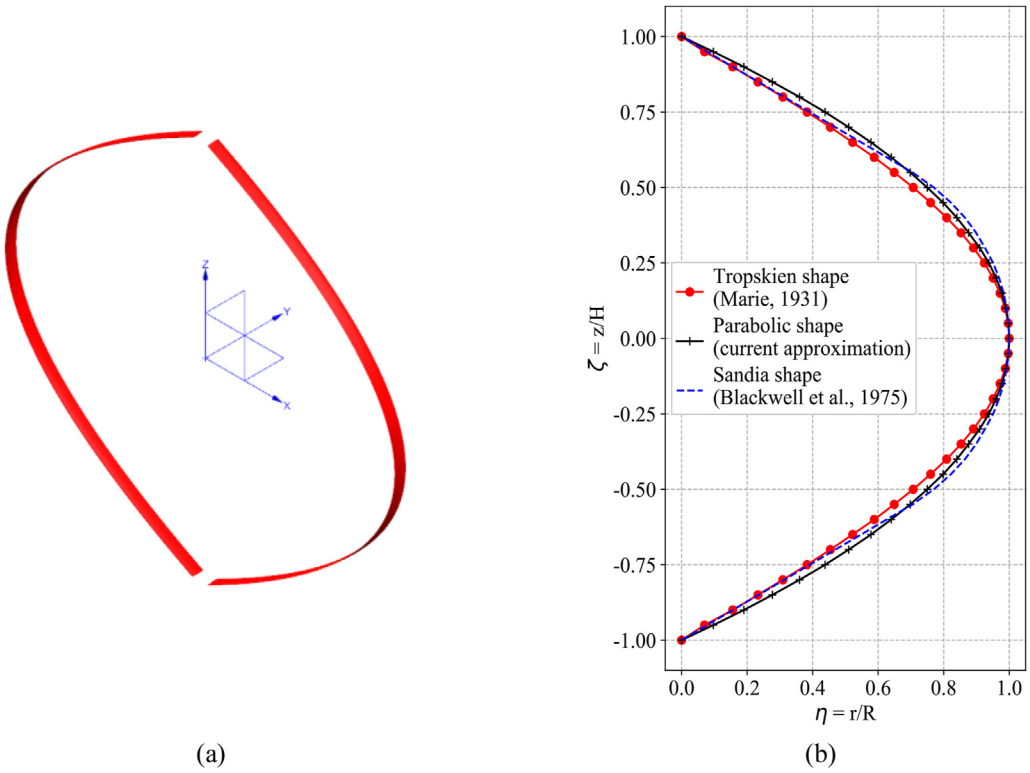

Fig. 1. (a) The isometric view of baseline two-blade model from Sandia 5m [27], neglecting the shaft and struts; (b) the approximations of ϕ-shape turbine blade by using Sandia shape [27] and parabolic shape.

Table 1
The configurations of the quadratic approximated model of ϕ-shape Darrieus turbine from the prototype of Sandia 5m [5].

Prototype	Sandia 5m
Airfoil	NACA0015
Chord length (mm)	152.40
Angular speed (rad/s)	17.07
Equatorial Radius (m)	2.50
Half-height (m)	2.55
Radius/Half-Height	0.98
Swept area (m^2)	17.01

2.2. Extension of the airfoil characteristics

A description of the pre-processing of the raw aerodynamic coefficients (C_d and C_l) for the airfoil is stated in this part. The raw airfoil characteristics [30] were in scattered form and the range of the angle of attack (AoA) was limited from 0° to 180° since they were initially tested for aircraft usage.

To fit the AoA range for VAWT use, the symmetrical extensions are conducted. As shown in Fig. 3 we extended the lift coefficient (C_l) by doing central symmetry at the point (0, 0), while we extended the drag coefficient (C_d) by doing axial symmetry about the axis of AoA = 0.

On the other hand, to make the data continuous (for DMST use), the curve-fit process is carried out. For AoA ranges from −40° to 40°, the linear interpolation is conducted. This is because the force coefficients are remarkably fluctuating within this range and the

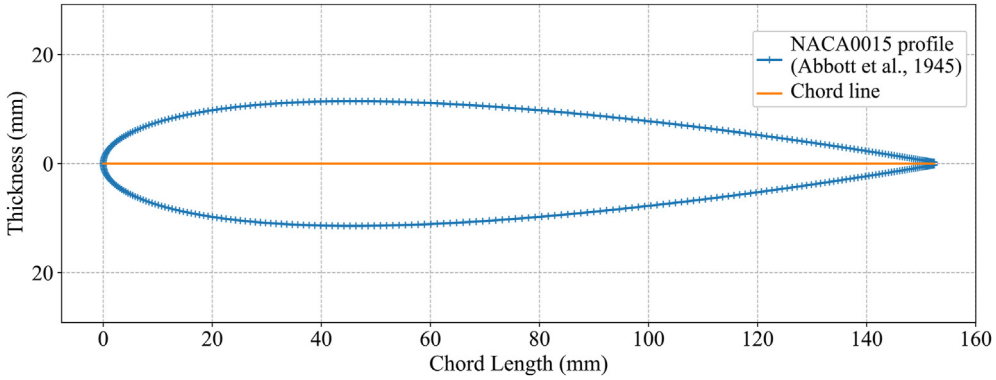

Fig. 2. The cross-section of the blade: NACA0015 airfoil [29] with a chord length of 152.4 mm.

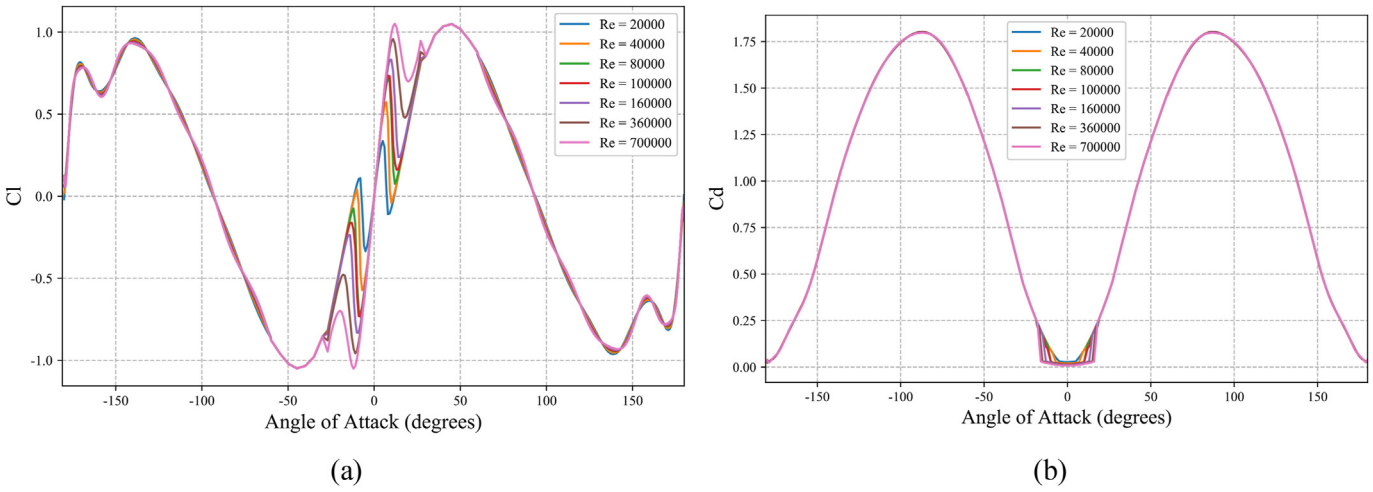

Fig. 3. The extension of the aerodynamic characteristics of NACA0015 airfoil: (a) lift coefficient: C_l (b) drag coefficient.C_d

original data has already been densely recorded (every 1°). For AoA ranges from −180° to −40° and 40° to 180°, where limited raw data was provided, high-order polynomial interpolation was further conducted to make the curve become smooth.

2.3. DMST model

Based on the BEM theory, the DMST model [20] is adopted for the aerodynamic simulation of ϕ-shape Darrieus turbine during the optimization process. Here, only the key content of the DMST model is introduced in this section.

Fig. 4 illustrates the plan view of the DMST model. The whole rotor cycle is cut into parallel strips, which are called the "streamtubes". Each streamtube is divided into three parts in tandem: The upwind-tube is in windward area while the downwind-tube is in the opposite side. In addition, the equilibrium zone is assumed as a connection placed in the middle of the streamtube.

At each elevation i, the inlet wind velocity V_i first entered into the upwind-tube and was reduced [20]:

$$V = uV_i \tag{3}$$

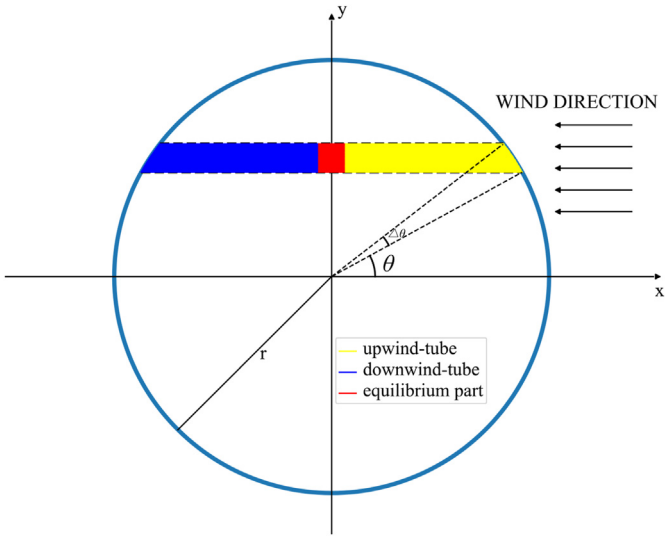

Fig. 4. The top view of the rotor in DMST model.

The induced factor u is derived through iteration using Formula (4), where f_{up} denotes the upwind function [20]:

$$u = 1 - \frac{f_{up}u}{\pi} \tag{4}$$

After obtaining the converged induced factor, by the double integral along the longitudinal and azimuthal directions, we can calculate the average power coefficient $\overline{C_{p1}}$ for the upwind part [20]:

$$\overline{C_{p1}} = \frac{R\omega}{V_\infty}\overline{C}_{Q_{up}} = \frac{R\omega}{V_\infty}\frac{BcH}{2\pi S}\int_{-\frac{\pi}{2}}^{\frac{\pi}{2}}\int_{-H}^{H} C_T\left(\frac{W}{V_i}\right)^2\left(\frac{r/R}{cos\delta}\right)dzd\theta \tag{5}$$

For the downwind part, the approach to get the average power coefficient $\overline{C_{p2}}$ can be analogically inferred. The final coefficient C_p is the sum of $\overline{C_{p1}}$ and $\overline{C_{p2}}$.

2.4. Consider desired range of inlet wind speed

The restriction of inlet wind range is important for VAWT design, as inlet wind range is always determined by the wind condition of the region where the VAWTs are installed. In this part, with a desired range of inlet wind speed, we attempt to fit our design by establishing a specific objective function for the optimization process. Note this is one of the innovation points of this work.

Generally, in order to ensure the optimization model is advanced to the baseline within a certain velocity range $[v_1, v_2]$ ($v_{opt} \in [v_1, v_2]$), the following constrains should be satisfied:

$$\forall v_i \in [v_1, v_2], \quad \frac{C_p(R, B, v_i, \beta)}{C_p(R_0, B_0, v_i, \beta_0)} > \lambda_{v_i} \tag{6}$$

where v_1 and v_2 denote the left bound and right bound of the desired optimal range, respectively. $v_1 < v_{opt} < v_2$; $C_p(R, B, v_i, \beta)$ is the power coefficient that calculated from DMST module at the inlet velocity v_i; R_0, B_0 and β_0 denote the settings of baseline; $\lambda_{v_i} \geq 1$ denotes the desired percentage of the improvement at the inlet velocity. v_i

Generally, the usage of CMAES algorithm is to find a numerical minimum for a non-convex target. In this paper, as we want to maximum C_p under the optimal velocity, the fitness was expressed

as its reciprocal:

$$f = 1/C_p^{'}(R, B, v_{opt}, \beta) \tag{7}$$

, where f denotes the output of the target function (i.e. the fitness in algorithm) and v_{opt} denotes the optimal velocity of the baseline turbine.

As for $C_p^{'}$, we intentionally proposed the following expression (8) to realize the specified wind range control during the numerical algorithm as below:

$$C_p^{'}(R, B, v_{opt}, \beta) = \psi\, C_p(R, B, v_{opt}, \beta) \tag{8}$$

The reduction factor $0 \le \psi \le 1$ is a punishment item for the unsatisfied samples. Hence the fitness of such instance would be larger during evolutionary process as long as its power coefficient is not fully optimized within the whole range. The expression of ψ is put as follows:

$$\psi = \prod_{v_i=v_1}^{v_2} \min\left(1, \frac{C_p(R, B, v_i, \beta)}{\lambda_{v_i} C_p(R_0, B_0, v_i, \beta_0)}\right) \tag{9}$$

In Formula (9), the denominator is the amplification of the difference of the unexpected cases. This expression has two meanings:

(i) It eliminates instances that do not meet the requirements in a given wind speed range, and the large the difference is, the greater the penalty will be added to its fitness, leading to an earlier elimination of such instances. This allows the algorithm to find the eligible design faster.

(ii) By setting different parameters $\lambda_{v_i} \ge 1$, it allows the user to have a focus in the design interval. For instance, although the user wants the optimized rotor to be suitable for inlet wind speeds from 5 m/s to 10 m/s, it is more desirable to ensure this optimization from 8 m/s to 10 m/s. In such case, λ_{v_i} for v_i from 8 m/s to 10 m/s should be tuned relatively larger than others.

It should be noticed that, for a given wind speed v_i, if the desired percentage λ_{v_i} is set to be an excessively large value, it will not be practically feasible. In another word, such design of turbine may not even exist under the DMST analysis. In that case, the results cannot be promised. However, the above expression still allows the algorithm return the output that is as close to the requirements as possible.

In addition, from previous papers [13,15,16,12,31], the number of intersection points by TSR-C_p curves of baseline and optimized turbine was no more than 2. This may indicate the optimization of the entire wind speed interval can be ensured only by using the boundary value of the wind speed range as constrains. Thus, Formula (9) becomes:

$$\psi = \min\left(1, \frac{C_p(R, B, v_1, \beta)}{\lambda_{v_1} C_p(R_0, B_0, v_1, \beta_0)}\right) * min\left(1, \frac{C_p(R, B, v_2, \beta)}{\lambda_{v_2} C_p(R_0, B_0, v_2, \beta_0)}\right) \tag{10}$$

Combining Formula(7), (8) and (10), we can obtain final objective function, which is the key step to control the VAWT design that fits the desired range of inlet wind speed during the optimization process.

2.5. *Process of CMAES*

The Covariance Matrix Adaptation Evolutionary Strategy (CMAES) [32] is used to accelerate the design process in this work. This optimization algorithm can be divided into three steps: Sampling, Selecting and Adapting. The explanatory flowchart is shown in Fig. 5 as below:

Every full circle begins with sampling, where we hope to choose the searching points that contain sufficient information to represent the generation they belong to. The distribution of sampling obeys Formula (11):

$$\boldsymbol{x}_k^{(g+1)} \sim \mathcal{N}\left(\boldsymbol{m}^{(g)}, {\sigma^{(g)}}^2 \boldsymbol{C}^{(g)}\right), k = 1, 2 \ldots \lambda \tag{11}$$

where g denotes the g^{th} generation and λ denotes the total number of samples for the generation; $\mathcal{N}(\boldsymbol{m}^{(g)}, \boldsymbol{C}^{(g)})$ represents a multivariate normal distribution.

2 Selecting

Each sample generated in the 1st step has its own fitness value. As we want to obtain the minimum solution, we rank them in ascending order and the first half are eligible to participate in updating new generations:

$$f(\boldsymbol{x}_{1:\lambda}) \le f(\boldsymbol{x}_{2:\lambda}) \le \ldots \le f(\boldsymbol{x}_{\lambda:\lambda}) \tag{12}$$

3 Adapting

The mean value $\boldsymbol{m}$, covariance matrix $\boldsymbol{C}$ and step-size σ are sequentially adapted through this step. Fig. 6 shows how the update proceeds.

First, the adapting of $\boldsymbol{m}$ is the vector addition of the differences between each preeminent individual (red dots in Fig. 5 (b)) and the original average (black rhombus in Fig. 5 (a)). Basically, this process is a "multi-recombination", which is similar to the "crossover" process in other derivative-free algorithms:

$$\boldsymbol{m}^{(g+1)} = \boldsymbol{m}^{(g)} + c_m \sum_{i=1}^{\mu} w_i \boldsymbol{y}_{i:\lambda}^{(g+1)} \sigma^{(g)} \tag{13}$$

, where $\boldsymbol{y}_{i:\lambda}^{(g+1)} = \frac{(\boldsymbol{x}_{i:\lambda}^{(g+1)} - \boldsymbol{m}^{(g)})}{\sigma^{(g)}}$, whose numerator is the step of the i^{th} sample and σ is the step-size; c_m denotes the learning rate for updating $\boldsymbol{m}$.

Instead of finding the gradient of the target function itself, CMAES transfers the parameters-objective mappings into a normal distribution and uses the stochastic sampling to estimate the corresponding natural gradient in order to search the best solution by

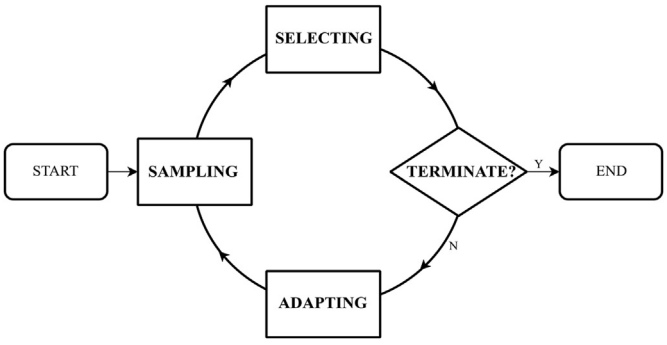

Fig. 5. Flow chart of CMAES algorithm, consisting three basic processes: sampling, selecting and adapting.

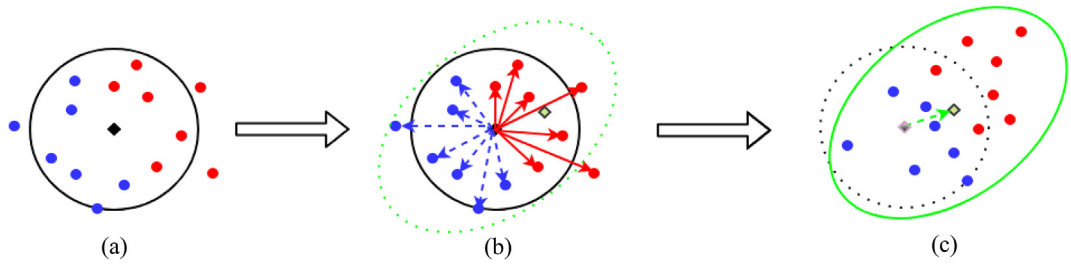

Fig. 6. The schematic process of adaptation in CMAES (taking 2-dimension problem as an example for illustration): (a) original multi-normal-distribution; (b) finding new center and covariance matrix, where red dots possess better fitness than blue ones; (c) adapted multi-normal-distribution.

natural gradient descent. This ideology is successively employed when updating the covariance matrix $\boldsymbol{C}$ using the steps of best μ samples.

$$\boldsymbol{C}_{rank-\mu}^{(g+1)} = (1-c_\mu)\boldsymbol{C}^{(g)} + c_\mu \sum_{i=1}^{\mu} w_i \left(\boldsymbol{y}_{i:\lambda}^{(g+1)}\right)\left(\boldsymbol{y}_{i:\lambda}^{(g+1)}\right)^T \tag{14}$$

where c_μ denotes the learning rate that retains a part of prior information for updating the next. $\boldsymbol{C}$

The step-size adapting makes the algorithm converge faster, and such technology is also known as the "cumulative step size adaptation" (CSA) (Hensan et al., 2006).

$$ln\sigma^{(g+1)} = ln\sigma^{(g)} + c_\sigma \left(\frac{\boldsymbol{p}_\sigma^{(g+1)}}{E\mathcal{N}(0,\boldsymbol{I})} - 1\right) \tag{15}$$

where c_σ denotes the learning rate for step-size control, $c_\sigma < 1$; $E\mathcal{N}(0,\boldsymbol{I})$ denotes the Euclidean norm of $\mathcal{N}(0,\boldsymbol{I})$ distribution; records the evolution path for step-size control.

2.6. Handle integer $\boldsymbol{p}_\sigma^{(g)}$ variable: the blade-number

In this study, among three variables which describe the shape of ϕ-shape turbine, the blade-number is an integer variable. However, the CMAES classically serves for variables that continuously change. To handle this, a useful trick proposed by Ref. [22] is adopted in this work.

We leave the blade-number change continuously in the real number domain in the Sampling and Adapting parts of CMAES. However, when evaluating the objective function in the Selecting part of CMAES, we truncate the value by the following expression:

$$B = \mathrm{INT}(B_{\mathrm{real}}) \tag{16}$$

where denotes the integer value of blade-number conveyed to the fitness calculation and $B$is the floating-point value of blade-number that continuously changes in other parts of the optimization process.

2.7. Overall framework and settings for the optimization program

The overaB_{real}ll framework involves the CMAES algorithm into DMST model, constructing an automatic program for the optimization of an ϕ-shape turbine to fit a given range of inlet wind speed.

As a summary of the methodology, the entire process of the program is illustrated in Fig. 7 as below, where the framework calls DMST module and CMAES module in iterate. All this work was based on a self-compiled script written on Python 3.6 platform and realized on a 4 cores computer with two Intel(R) Xeon(R) CPUs (E5-2673 v4), taking less than 1 s to evaluate a single instance.

It should be noticed that, setting adequate initial conditions as well as the feasible boundaries for the parameters are significantly important for CMAES. Most of the crucial settings are listed in Table 2, where the initial means and were tuned by randomly restarting from different settings in order to avoid dropping into local minimal results. Since the chord length for the current case is unchanged, the total size of the turbine should be correspondingly contained within a reasonable space. Moreover, the right bound of inlet velocity should not be too large because of theσ_0 limitation of using BEM during high dynamic stalls.

3. Results

As results, two sub-parts are included in this section. In the first part, the verification of the current program using the prototype, Sandia 5m, is presented. In the second part, the optimization results compared with the baseline are discussed.

3.1. Baseline verification

A validation is firstly conducted to test feasibility of the aerofeatures of NACA0015 airfoil after the pre-processing, since the outputs based on DMST model are highly dependent on the aerodynamic characteristics of the airfoil.

Fig. 8 illustrated the windward and leeward normal force coefficients for Sandia 5m, which were calculated from the current code (solid line) and the reference (dotted line) [20]. The estimated curves match well with the referred lines for both windward and leeward parts extracted from Refs. [20]. Only small bias exists when it approaches the maximum normal force, corresponding to a high local Reynolds number and a relatively low AoA. The possible reasons may be the differences between SCS (adopted by reference) and parabolic (adopted by current paper) approximations in the height level and the different sources and interpolation treatments regarding to the discrete values of C_l and C_d .

In Fig. 9, a full range of TSR comparison (from 1 to 9) of the power coefficient for the baseline between the current prediction and the site data carried out by Sandia Laboratory is plotted [5]. As a supplementation, the result of CARDAA code is also added (Paraschivoiu, 1981). It should be noticed that, although the site measurement and the code data have been released for nearly 40 years, the reliability have been abundantly validated by previous researchers [33–37].

Fig. 9 shows that the present prediction and experimental results are in good agreement for TSR from 3.5 to 8.0 and the current results almost overlapped with that of the CARDAA code within TSR from 4 to 7.5. The largest C_p from site data is 0.332 when TSR equals to 5.53, where the velocity is equal to 7.68 m/s. However, the current code slightly underestimates the performance when it comes to low TSRs while overestimation appears when TSR becomes large. In another words, the performance curve computed based on the BEM theory is subtly right-shifted, reaching a maximum of 0.337 at

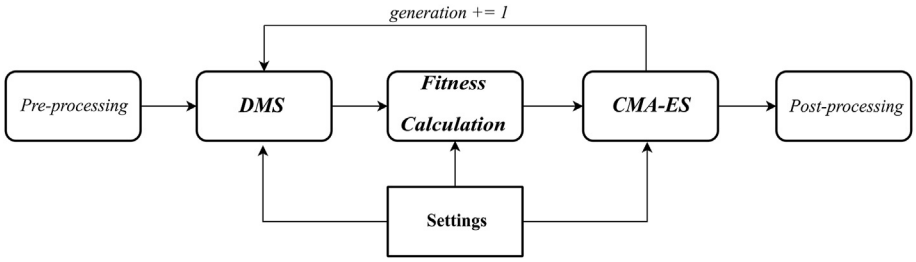

Fig. 7. Overall structure of the ϕ-shape turbine shape optimization program based on DMST and CMAES modules.

Table 2
Variants space, initial conditions and other settings of the whole optimization program.

Variants space	R	$0 < R < 5$
	B	$0 < B < 5$
	β	$0 < \beta < 2$
Desired inlet range	v_1	5
	v_2	10
Initial means	R_0	2.5
	B_0	2.5
	β_0	1
Hyper-parameters	σ_0	1.7
	λ	10
	$\lambda_{v_1}, \lambda_{v_2}$	1
	Learning rates	32

an inlet wind speed of 7.24 m/s. One reason accounting for this phenomenon may be the site experiment was conducted in a high altitude [27], where the general inlet wind velocities along elevation were larger than the wind profile we assumed in BEM. Another main cause might be that the current model does not take the effects of struts into consideration, which will scale the inlet velocities and shift the performance curve to a higher wind speed as a result.

3.2. Optimization results

The shape optimization is conducted under the target wind inlet of 7.68 m/s, which is the optimal wind speed of baseline. Other settings of the algorithm are in accordance with Table 2, where the desired wind speed range is set to be 5 m/s to 10 m/s. Fig. 10 illustrates the changes of the means of the shape parameters through first 20 generations (i.e. 200 times of evaluations for the population size equals to 10). It should be noticed that in Fig. 10 the blade-number is round down to integer however during iterations this value was changing continuously (see Formula 16).

Fig. 11 shows the relationship between Standard Deviations (SD) and Numbers of Iteration (NI) for the parameters of radius,

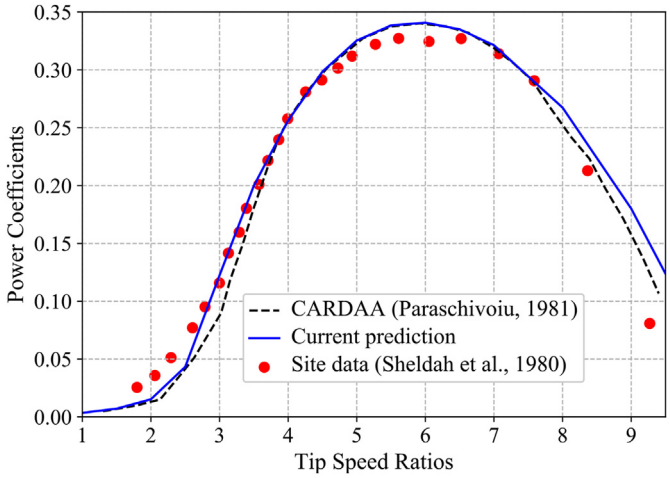

Fig. 9. Power coefficient versus the tip speed ratio for the non-optimized model compared with references from CARDAA [38] code and site data [5].

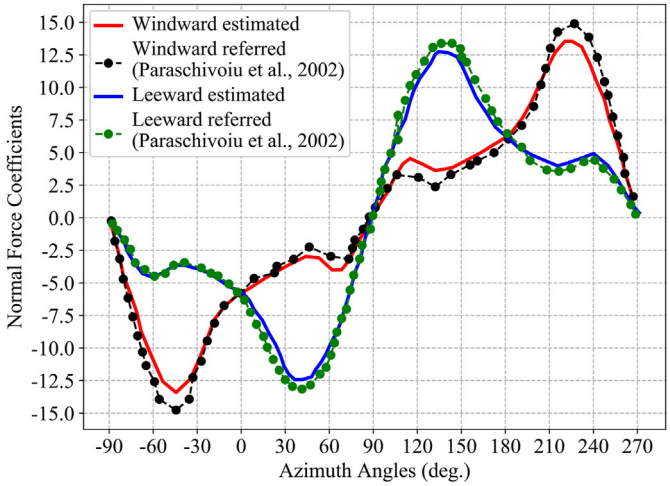

Fig. 8. Variations of normal force coefficient for two-blade Sandia 5m with azimuth angle, TSR = 3.0. Comparisons on the normal force coefficients of the windward and leeward sides between the current study and reference [20].

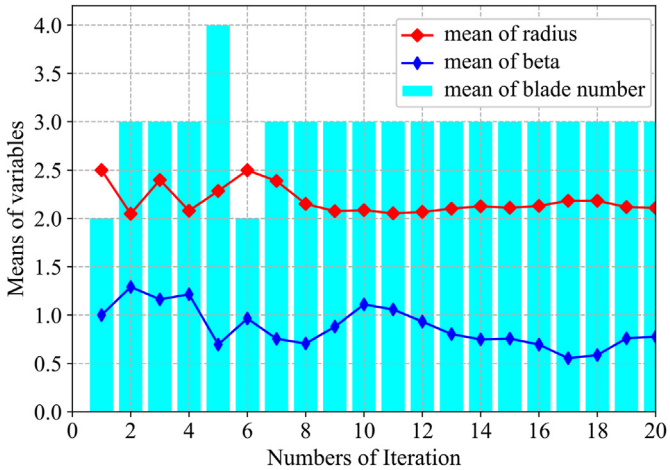

Fig. 10. Variations of the average of three variables during the first 20 generations iterated by CMAES algorithm (population size = 10, inlet wind velocity = 7.68 m/s).

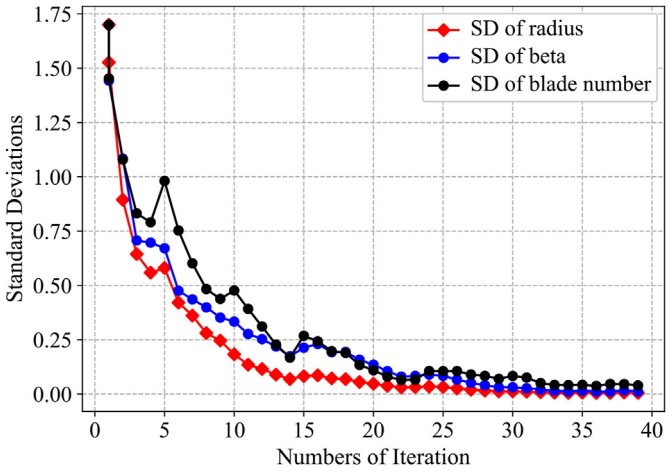

Fig. 11. Variations of the SD (= standard deviation) of three variables during the whole 40 generations iterated by CMAES algorithm (population size = 10, inlet wind velocity = 7.68 m/s).

diameter-height ratio and blade-number. SD reflects the degree of geometrical difference of the turbine models in the sample space of each generation, while NI is plotted to describe the development of the evolution process. It could be found from Fig. 11 that all the trends of the radius (red), diameter-height ratio (blue) and blade number (black) are decreasing and gradually approaching to zero. This represents that the optimization process is converged.

Different plane-view of the comparison between the final evolved shape (blue) and the virginal shape (red) are shown in Fig. 12. As plotted in Fig. 12 (a) and 12 (b), the optimized model from the DMST-CMAES process has a shorter radius, equaling to 2.12 m and a smaller diameter-height ratio of 0.76 (scilicet a larger height of 5.62 m). As plotted in Fig. 12 (c), the blade-number has been changed from two to three. Fig. 12(d) compares the isometric views between the optimized and non-optimized model, where the swept area of the new rotor is 15.89 m^2, which is 93.39% of that of the non-optimized rotor.

Since the turbine radius is changed after the shape optimization, to illustrate the improvements of power efficiency more clearly related to the given inlet ranges, we will plot $C_p - v_\infty$ instead of standard $C_p - TSR$ graph in the next contents. As a result shown in Fig. 13, the shape from the current code has an optimized C_p of 0.374 under the inlet wind velocity of 7.68 m/s. Meanwhile, this model successfully improved the rotor's performance within the entire expected wind range (i.e. from $v_1 = 5.0$ m/s to $v_2 = 10.0$ m/s). The best inlet wind speed for the optimized model was left-shifted to 7.11 m/s, reaching a peak C_p of 0.384. The largest percentage of C_p improvement occurred at the inlet wind speed of 6.52 m/s, with an enhancement of 15.49%. Though the evolved optimal wind speed is no longer the most suitable speed for the original model, the new model still raised the power coefficient of the prototype by 12.5% under its best inlet wind velocity at 7.68 m/s, which is a noticeable enhancement.

Fig. 14 also compares the C_p curves between the base model and the optimized mode, however, without adding desired interval of wind speed as constrain during the optimization process. The power coefficient of such design exceeds 0.4 at the optimum wind speed (7.68 m/s), and the percentage of improvement is higher than 30% when wind speed approaches 10 m/s. Nevertheless, for the interval of 5 m/s to 6 m/s, its performance is inferior to the original model, and the C_p value is even less than half of that of the prototype at 5 m/s. Therefore, without considering wind speed constrains, though the increase at optimal speed could be globally larger, the optimized scope cannot be controlled.

In addition, Fig. 15 shows the comparison of optimized C_p curves with different inlet wind ranges as limitations (Table 3). First, it can be referred that all C_p curves successfully surpass the baseline model within its given wind range. Also, these C_p curves in Fig. 15 present a converging trend while the given wind range become smaller, until approaching the no-restriction C_p curve. In addition, as the restriction of inlet wind range become stricter (wider), the C_p values at the target wind speed (7.68 m/s) are decreasing, indicating that a larger optimal range will lead to a sacrifice of the improvement at the target wind speed.

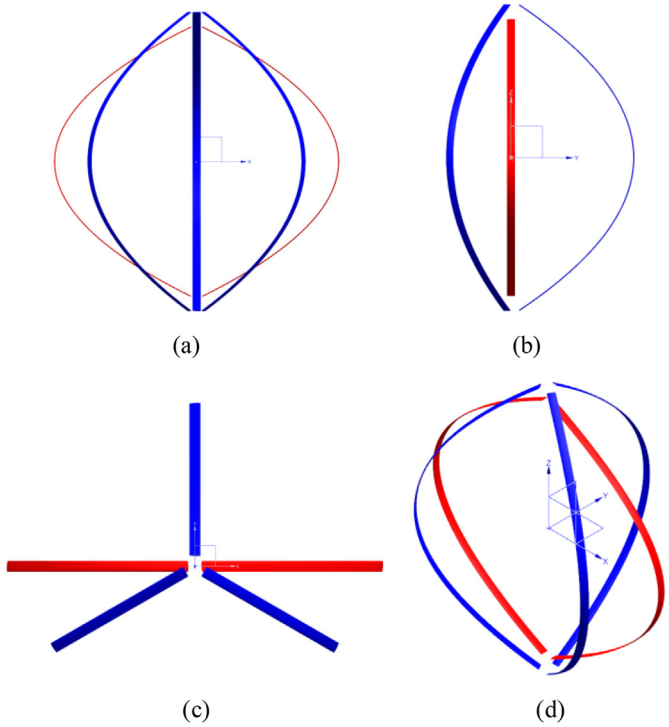

Fig. 12. Comparison of the optimized (blue) and non-optimized (red) VAWT shapes: (a) Front view; (b) Right-side view; (c) Top view; (d) Isometric view.

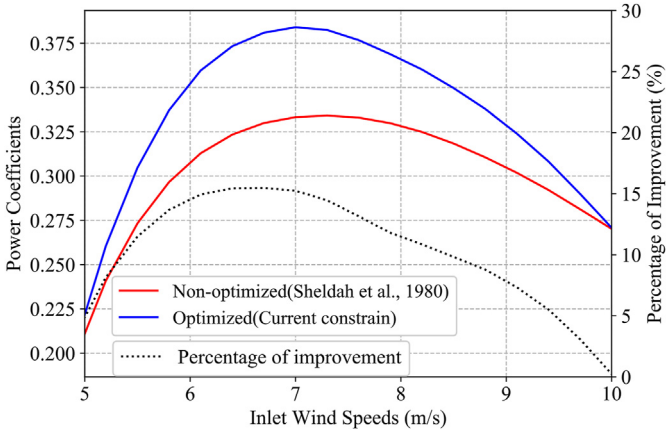

Fig. 13. Comparisons of C_p between optimized (with inlet wind constrains) and non-optimized [5] models with inlet wind velocity range varying from 5.0 m/s to 10.0 m/s.

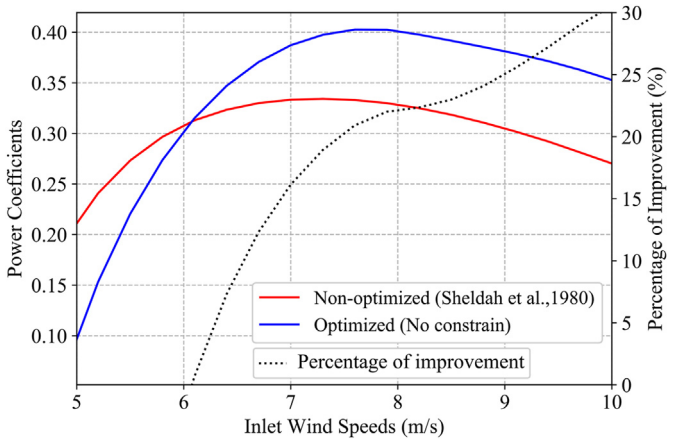

Fig. 14. Comparisons of C_p between optimized (without inlet wind constrains) and non-optimized [5] models with inlet wind velocity range varying from 5.0 m/s to 10.0 m/s.

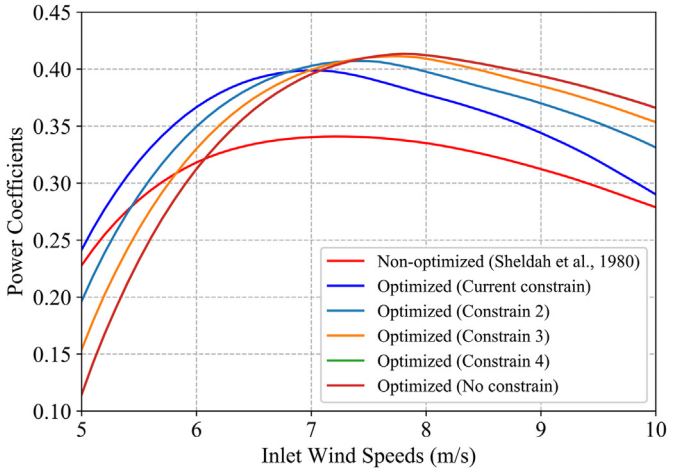

Fig. 15. Comparisons of the baseline C_p curve and optimized C_p curves under different inlet wind constrains

4. 3D CFD validation

Since the streamtube model can only reflect the time-averaged features of the flow field during rotations (Ferreira 2009), a three-dimensional CFD validation for the optimized rotor is here conducted as a supplement. The geometry of the model is shown in Fig. 12, with a maximum diameter in its equatorial plane equaling to 4.24 m and a total height of 5.62 m. Its airfoil has a chord length of 152.4 mm and the type of the profile is NACA0015. The working condition is under the inlet wind speed of 7.68 m/s with rotor rotating at 17.07 rad/s.

4.1. Layout and boundary conditions

The layout of the optimized three-blade ϕ-type wind turbine with the CFD simulation is shown in Fig. 15. The computational domain was divided into a rotation zone and static zone by creating interfaces. As shown in Fig. 16(a) and (b), the length, width and height of the whole domain were 17D, 10D and 4D in total. The rotation domain has a spindle-shaped outline, which is designed to reduce the computational cost. A quadratic curve similar to the contour of the blade was used to create such rotation region, and the equatorial diameter of the rotation domain is 1.5 times of that of the turbine. Based on the published studies [39–41], this size of the rotation domain was considered large enough for VAWT analysis.

As for the boundary conditions, according to the suggestions from former researches [13,39,42], the left bound (5D from the center of turbine) and the top bound (2D above the turbine center) were set as the velocity inlet, from which the wind was uniformly imported towards the positive-x direction. The pressure outlet was12D downstream from the center of turbine to make the wake fully developed. The front and back sides (both 5D from the turbine center) in Fig. 16 (a) were set as the symmetric planes and the bottom bound (2D beneath the turbine center) in Fig. 16 (b) was set as a no-slip wall.

4.2. Numerical settings

Numerical settings for the 3D CFD validation of the optimized ϕ-turbine are stated as follows. The finite volume method (FVM) was used to conduct the three-dimensional simulation of unsteady incompressible flow. The implicit unsteady segregated flow method was adopted to solve the continuity and momentum equations, and the SST k-ω turbulence model was chosen to resolve the N–S equations for its advantages in dealing flow around boundary layers.

The first-order central difference scheme was selected as the temporal discretization. We adopted SIMPLE scheme to couple the RANS model and the pressure-velocity equation. The sliding mesh technique was used to perform the motion of rotation. The increment of azimuth angle was 2° hence time-step was 1/180 of the period, which has been proved to be small enough for VAWT simulation [43]. The number of maximum inner iterations was 15 and the simulation terminated when the maximum physical time was larger than eight periods. The simulation was based on the platform of "Star CCM+ 13.04" software and it took about 216 h per instance for a 44 cores Serve with two Intel(R) Xeon(R) CPUs (E5-2673 v4) to complete the computation.

4.3. Mesh settings and grid independence analysis

The mesh topology and the grid independence test for the CFD simulation of the optimized ϕ-turbine are discussed in this part. Before all, several dimensionless parameters to evaluate the results are first presented as follows:

$$C_Q = \frac{Q}{\rho S R_{eq} {V_\infty}^2 / 2} \tag{17}$$

$$X_{eq} = \omega R_{eq} / V_\infty \tag{18}$$

Table 3
Different constrains of given inlet wind range in Fig. 15

	Current Constrain	Constrain 2	Constrain 3	Constrain 4	Constrain 5
v_1 (m/s)	5	5.5	6	7	No constrain
v_2 (m/s)	10	9.5	9	8	No constrain

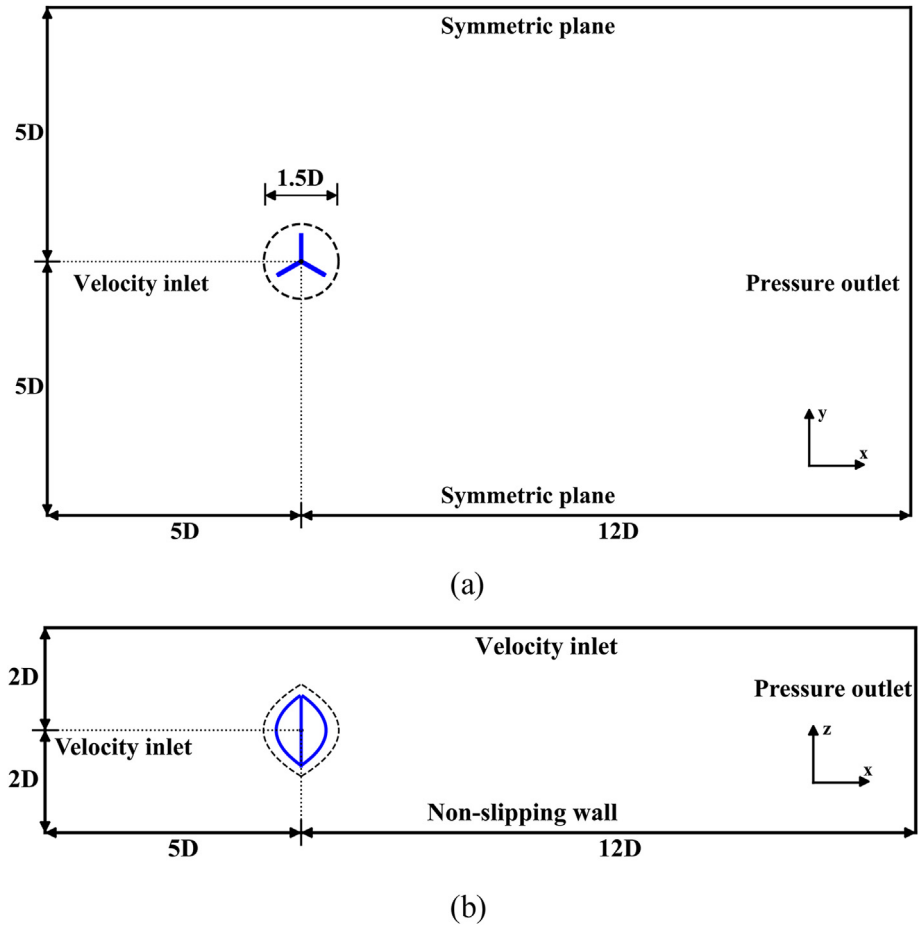

Fig. 16. The layout of the computational domain (D is the diameter of turbine): (a) top view; (b) front view; the dashed line covering the turbine (blue solid line) was the rotational zone, which was designed as a shape of spindle apparatus to minimize the cell needed.

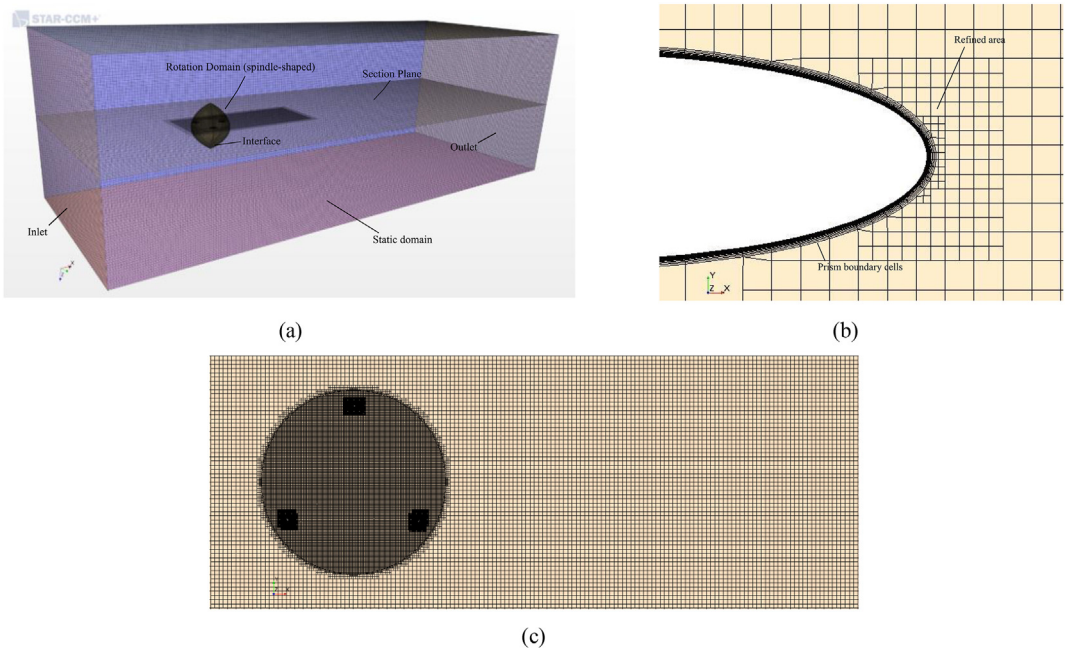

Fig. 17. Mesh topology for the CFD simulation of the optimized ϕ-shape VAWT: (a) whole mesh topology; (b) boundary layer grids around blade; (c) refined part in equatorial section plane.

Table 4
Different mesh settings around the blade.

Mesh Type	Minimum Grid Size	Total Cell Number	Difference of Cell Number	Difference of C_p
Coarse Mesh	0.001 m	26.44 million	- 30.57%	- 5.54%
Medium Mesh	0.00075 m	34.15 million	- 10.33%	- 0.63%
Fine Mesh	0.0005 m	38.08 million	0%	0%

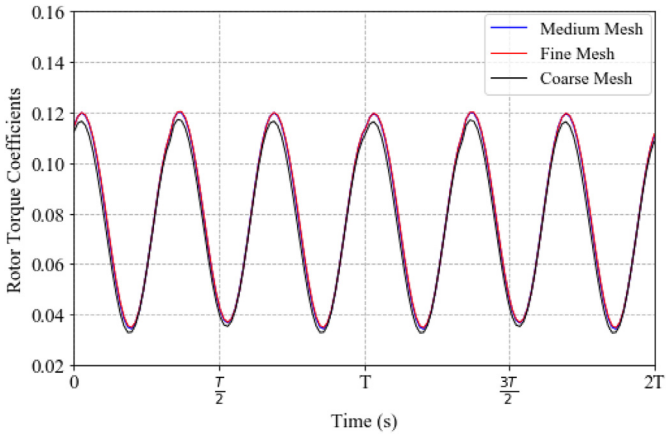

Fig. 18. The comparison between three mesh schemes in terms of rotor torque coefficients in the last two periods.

$$C_p = \frac{\overline{Q} X_{eq}}{\rho S R_{eq} {V_\infty}^2 / 2} = \overline{C_Q} X_{eq} \tag{19}$$

where C_Q is the torque coefficient; X_{eq} is the tip speed ratio of the equatorial plane; C_p is the power coefficient of the rotor; Q denotes the instantaneous rotor torque; ρ denotes the ambient air density, set to be 1.18 kg/m^3 at one standard atmosphere, 25 °C; S denotes the swept area of the turbine, which equals to 15.89 m^2 for the optimized model; R_{eq} is the equatorial rotor radius, which equals to 2.12 m; V_∞ denotes the inlet wind velocity, which equals to 7.68 m/s; ω denotes the angular speed of the rotor, which equals to 17.07 rad/s; $\overline{Q}$ and $\overline{C_Q}$ denote the mean rotor torque and the mean torque coefficient of the last two periods after the calculation becomes steady.

Fig. 17 shows the entire mesh topology and the boundary layer grids around the leading edge of the blade. The trimmed mesher was used for the cell generation for both stationary and rotational

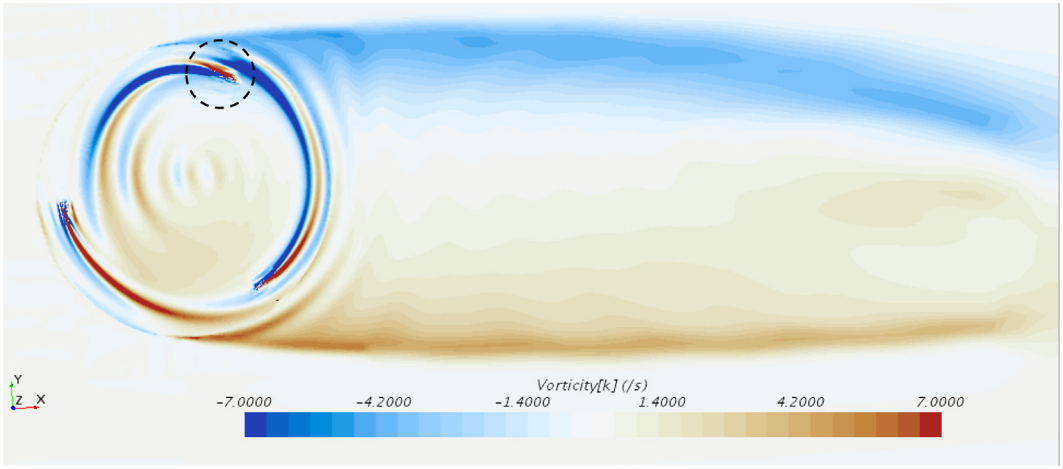

(a)

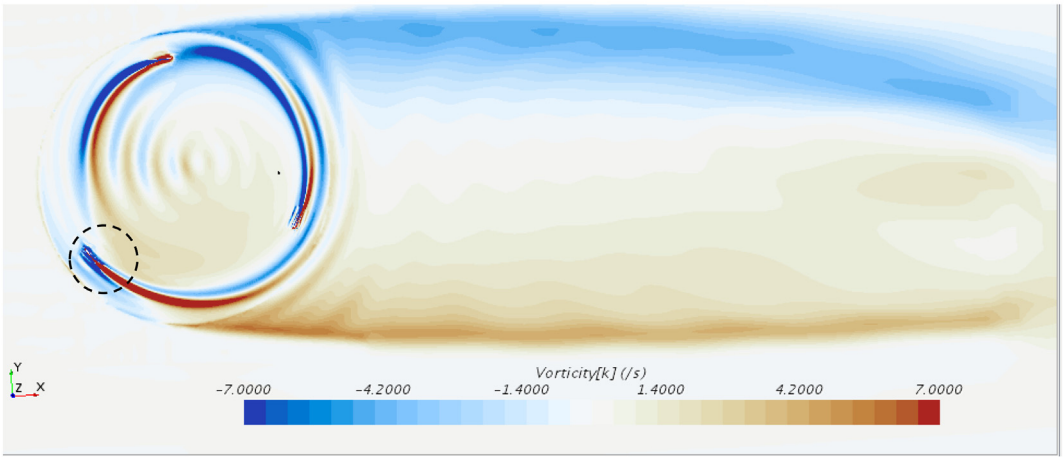

(b)

Fig. 19. The wake structures on the equatorial section (R = 2.12m) for the optimized ϕ-shape turbine by adopting SST. k-ω turbulence model (v = 7.68 m/s): (a) θ = 24.40°; (b) θ = 234.67°.

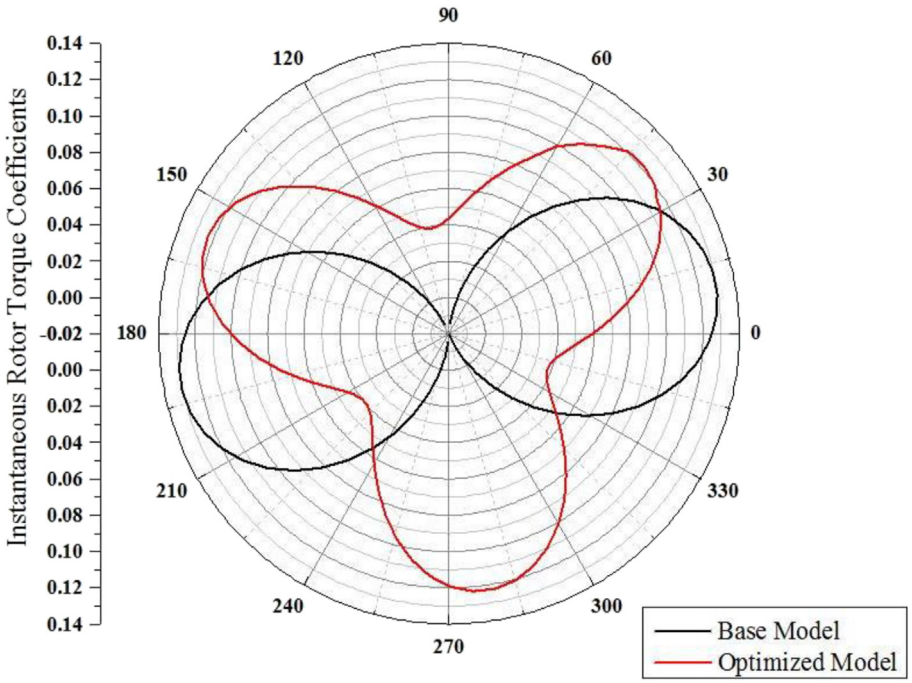

Fig. 20. Comparison of the instantaneous rotor torque coefficients between the base model and the optimized model using 3D CFD method.

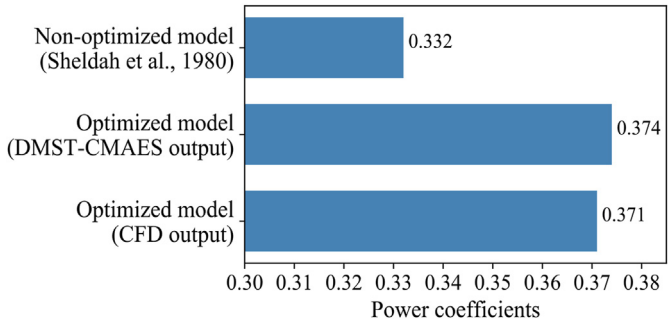

Fig. 21. Comparisons of power coefficients from the non-optimized model [5] and optimized model (from DMST code and CFD method) under the inlet wind velocity of 7.68 m/s.

domain while for the blade surfaces in the rotational zone, the prismatic layer mesher was additionally adopted. The number of mesh achieved 34.15 million in total, with the minimum grid size of blades equal to 7.5e-4 m. This quantity is considerably large because the equatorial diameter of the rotor is over 4240 mm while the airfoil chord length is only 152.4 mm, giving a tiny chord-diameter ratio of 0.036. As a result, the size of the prismatic boundary cell should be small enough to meet the requirement of $y^+ \approx 1$, and this leads to a comparatively larger growth rate from the boundary-layer to rectangular cells in Fig. 17 (b). To be specific, the total thickness of the 20 prismatic boundary layers is 0.001 m and the growth rate of the boundary layer is set to be 1.2 in this study.

There is a trade-off between the accuracy and the computational time by using different mesh sizes. In this study, the mesh dependence test was conducted by changing the minimum grid size around the blades. The properties of using three types of meshes, named as “Coarse Mesh”, “Medium Mesh”, and “Fine Mesh”, are presented in Table 4. It can be found that the difference of the power coefficients from medium mesh and fine mesh was tiny enough while the total number of the refined grids was 10.33% larger. On the other hand, the coarse mesh was lack of adequate accuracy. With the definition of the torque coefficient C_Q defined in Formula (17), a time-history of the last two periods of C_Q under different mesh schemes is shown in Fig. 18, where a distinguished difference of C_Q values can be found between the coarse mesh and the other two meshes. Therefore, we choose the “Medium Mesh” scheme for the simulation.

4.4. Comparisons

Though wake properties cannot be described by DMST algorithm, it is available in CFD simulation. As shown in Fig. 19, the vortex structures of the optimized turbine at different rotor positions can be depicted by SST k-ω turbulence model. The wake detached in clockwise direction from the leading edge, forming a negative vortex street (blue, Fig. 19 (a)) on the upper side while anticlockwise vortex appears on the other (red, Fig. 19 (b)) with positive values. Similar observations have also been found in other CFD analysis of VAWTs [43].

After eight-period calculation, the residual error was lower than 0.0001 and the output had become steady (see Fig. 18, the difference between the adjacent periods was less than 1%). Fig. 20 compares the azimuthal variation of the instantaneous rotor torque coefficients for the base model and the optimized model. It can be found that despite a slight decrease of the peak values, the negative parts of C_Q were totally eliminated during the optimization, which contributes to the entire increase of the rotor efficiency. Similar observation was also found by previous researchers [44].

The mean rotor torque coefficient of within a period was further plugged into Formula (19) to calculate the power coefficient, giving a C_p value of 0.371 under the inlet wind velocity of 7.68 m/s. As shown in Fig. 21, compared with the DMST output of 0.374, this result shows a good consistency. Hence, at this point, it validates the former prediction for the optimized model. The power coefficient for the non-optimized model was also plotted to show the

improvements and an 11.7% enhancement was found between the power coefficients of the optimized model from CFD output and the non-optimized model from the experimental test.

Regarding the computational cost, the time cost to obtain the optimized model by using DMST-CAMES framework takes less than 1 h, with more than 150 evaluations completed during the process. While it takes more than 200 h to conduct the validation for a single instance by using 3D CFD method. Because of the considerable computational cost, there is a limitation of lacking other validations for different inlet wind speeds.

5. Conclusions

Through the current work, a rapid shape optimization of an ϕ-shape Darrieus wind turbine was conducted on the basis of the BEM theory and CMAES algorithm to achieve an entire improvement under a given range of inlet wind speed. The base model is two-blade Sandia 5m, with a maximum power coefficient of 0.332 under the inlet wind speed of 7.68 m/s. After 40-generation evolution, the efficiency of the turbine was 12.5% higher with the radius reduced from 2.50 m to 2.12 m, the height increased from 5.10 m to 5.62 m and the blade-number changed to 3 in the end.

Essential conclusions can be made as follows:

1. Coupling DMST model and CMAES algorithm can successfully find an improved shape for a given ϕ-shape VAWT prototype under a desired inlet wind velocity.
2. By setting appropriate objective function for the optimization algorithm, the program can guarantee that the improvements occur everywhere in a given range of inlet wind speed.
3. Through 3D CFD validation based on SST k-ω turbulence model, it is proved that this work can not only largely speed up the process of optimization process, but also can provide a reliable accuracy.

The method from current study may be applied in the preliminary shape design of ϕ-shape Darrieus turbine. In the future, following works could be implemented as amelioration:

1. Try different extending methods, including different interpolation schemes, of the raw dataset regarding the lift and drag coefficients.
2. Revise the BEM based code by choosing appropriate stall models to acquire a more accurate prediction.
3. Try different analogy model of the Troposkien shape and conduct the shape optimization by changing parameters of their shape functions.
4. Parameterize other influences from the model to improve the performance of Darrieus wind turbine, such as the profile of the cross-section, the shape of the shaft and struts, etc.
5. For both base model and optimized model, explore their aerodynamic features, including wake structures, under other inlet speeds using 3D CFD method, and make comparison with the DMST outputs.

Acknowledgements

The financial supports from the Innovation Program of Shanghai Municipal Education Commission (No.:2019-01-07-00-02-E00066), National Natural Science Foundation of China (Nos. 51879160, 51809170, 11772193 and 51679139), Shanghai Natural Science Foundation (Nos. 17ZR1415100 and 18ZR1418000), and Project of Thousand Youth Talents are gratefully acknowledged. This research is also sponsored in part by Program for Professor of Special Appointment (Eastern Scholar) at Shanghai Institutions of Higher Learning (Nos. ZXDF010037 and ZXDF010040), Program for Intergovernmental International S&T Cooperation Projects of Shanghai Municipality (No.18290710600), and Program for International Cooperation of Shanghai Science and Technology (No.18160744000).

References

[1] Y. Wang, H. Tong, H. Sima, J. Wang, J. Sun, D. Huang, Experimental study on aerodynamic performance of deformable blade for vertical axis wind turbine, Energy 181 (2019) 187–201.
[2] M. Jafari, A. Razavi, M. Mirhosseini, Effect of airfoil profile on aerodynamic performance and economic assessment of H-rotor vertical axis wind turbines, Energy 165 (2018) 792–810.
[3] S. Eriksson, H. Bernhoff, M. Leijon, Evaluation of different turbine concepts for wind power, Renew. Sustain. Energy Rev. 12 (5) (2008) 1419–1434.
[4] B. Blackwell, G. Reis, Blade shape for a tropskien type of vertical-axis wind turbine, in: Sandia Labs, NM (USA), Albuquerque, 1977. Retrieved from.
[5] R.E. Sheldahl, P.C. Klimas, L.V. Feltz, Aerodynamic performance of a 5-metre-diameter darrieus turbine with extruded aluminum NACA-0015 blades: national technical information service USA, 1980.
[6] M.A. Singh, A. Biswas, R.D. Misra, Investigation of self-starting and high rotor solidity on the performance of a three s1210 blade h-type darrieus rotor, Renew. Energy 76 (2015) 381–387.
[7] Q. Li, T. Maeda, Y. Kamada, J. Murata, K. Shimizu, T. Ogasawara, et al., Effect of solidity on aerodynamic forces around straight-bladed vertical axis wind turbine by wind tunnel experiments (depending on number of blades), Renew. Energy 96 (pt) (2016) 928–939.
[8] Y. Wang, S. Shen, G. Li, D. Huang, Z. Zheng, Investigation on aerodynamic performance of vertical axis wind turbine with different series airfoil shapes, Renew. Energy 126 (OCT.) (2018) 801–818.
[9] M. Mohamed, Performance investigation of H-rotor darrieus turbine with new airfoil shapes, Energy 47 (1) (2012) 522–530.
[10] Bianchini Alessandro, Balduzzi Francesco, M. John, An experimental and numerical assessment of airfoil polars for use in darrieus wind turbines-part I: flow curvature effects, in: Proceedings of the ASME Turbo Expo 2015: Turbine Technical Conference and Exposition. Volume 9: Oil and Gas Applications; Supercritical CO2 Power Cycles; Wind Energy, Canada, Montreal, Quebec, 2016. June 15–19, 2015. V009T46A006.
[11] M.Y. Sun, D.Y. Kim, J.K. Lim, Study on optimal design of wind turbine blade airfoil and its application, Transactions of the Korean Society of Mechanical Engineers B 36 (5) (2012) 465–475.
[12] T.J. Carrigan, B.H. Dennis, Z.X. Han, B.P. Wang, Aerodynamic shape optimization of a vertical-axis wind turbine using differential evolution, ISRN Renewable Energy 2012 (2012) 1–16.
[13] N. Ma, H. Lei, Z. Han, D. Zhou, Y. Bao, K. Zhang, C. Chen, Airfoil optimization to improve power performance of a high-solidity vertical axis wind turbine at a moderate tip speed ratio, Energy 150 (2018) 236–252.
[14] G. Bedon, M.R. Castelli, E. Benini, Optimization of a darrieus vertical-axis wind turbine using blade element–momentum theory and evolutionary algorithm, Renew. Energy 59 (2013) 184–192.
[15] G. Bedon, M.R. Castelli, E. Benini, Optimal spanwise chord and thickness distribution for a troposkien darrieus wind turbine, J. Wind Eng. Ind. Aerod. 125 (2014a) 13–21.
[16] G. Bedon, M.R. Castelli, E. Benini, Proposal for an innovative chord distribution in the Troposkien vertical axis wind turbine concept, Energy 66 (2014b) 689–698.
[17] G. Bedon, E. Benini, Aero-structural design optimization of vertical axis wind turbines, Wind Energy 20 (3) (2017) 491–505.
[18] C.M. Chan, H.L. Bai, D.Q. He, Blade shape optimization of the savonius wind turbine using a genetic algorithm, Appl. Energy 213 (2018) 148–157.
[19] E. Antar, M. Elkhoury, Parametric sizing optimization process of a casing for a savonius vertical axis wind turbine, Renew. Energy 136 (2019) 127–138.
[20] I. Paraschivoiu, Wind turbine design: with emphasis on darrieus concept: presses inter Polytechnique, 2002.
[21] N. Hansen, S.D. Müller, P. Koumoutsakos, Reducing the time complexity of the derandomized evolution strategy with covariance matrix adaptation (CMA-ES), Evol. Comput. 11 (1) (2003) 1–18.
[22] S. Rahnamayan, P. Dieras, Efficiency competition on N-queen problem: DE vs. CMA-ES. Paper presented at the 2008 Canadian conference on electrical and computer engineering, 2008.
[23] M. Hasenjäger, B. Sendhoff, T. Sonoda, T. Arima, Three dimensional evolutionary aerodynamic design optimization with CMA-ES. Paper presented at the proceedings of the 7th annual conference on genetic and evolutionary computation, 2005.
[24] A. Athanasiou, M. De Felice, G. Oliveto, P.S. Oliveto, Evolutionary algorithms for the identification of structural systems in earthquake engineering. Paper presented at the IJCCI (ECTA-FCTA), 2011.
[25] A. Rossetti, G. Pavesi, Comparison of different numerical approaches to the study of the H-Darrieus turbines start-up, Renew. Energy 50 (2013) 7–19.
[26] P.-L. Delafin, T. Nishino, A. Kolios, L. Wang, Comparison of low-order aerodynamic models and RANS CFD for full scale 3D vertical axis wind turbines,

Renew. Energy 109 (2017) 564–575.
[27] B. Blackwell, G. Reis, Geometrical aspects of the troposkien as applied to the darrieus vertical-axis wind turbine, Design Engineering Technical Conference 5 (1975) 17–19.
[28] D.G.J. Marie, Turbine having its rotating shaft transverse to the flow of the current. In: google Patents, 1931.
[29] I.H. Abbott, Von Doenhoff, A.E., L. Stivers Jr., Summary of airfoil data, 1945.
[30] R.E. Sheldahl, P.C. Klimas, Aerodynamic characteristics of seven symmetrical airfoil sections through 180-degree angle of attack for use in aerodynamic analysis of vertical axis wind turbines, Retrieved from. Sandia National Labs, NM (USA), Albuquerque, 1981.
[31] R. Kemp, Airfoil Otimization for Vertical Axis Wind Turbines, Airfoil Otimization for Vertical Axis Wind Turbines (2015).
[32] N. Hansen, The CMA evolution strategy: a tutorial. *arXiv preprint arXiv: 1604.00772*, 2016.
[33] A.A. Mohammed, H.M. Ouakad, A.Z. Sahin, H.M. Bahaidarah, Parametric study and comparison of aerodynamics momentum-based models for straight-bladed vertical axis wind turbines, Arabian J. Sci. Eng. 45 (2) (2020) 729–741.
[34] D. Hilewit, E. Matida, A. Fereidooni, H. Abo el Ella, F. Nitzsche, Numerical investigations of a novel vertical axis wind turbine using Blade Element Theory-Vortex Filament Method (BET-VFM), Energy Science & Engineering 7 (6) (2019) 2498–2509.
[35] H.T.H. Le, C.C. Nguyen, T.H. Luong, Performance prediction of darrieus vertical axis wind turbines using double multiple stream-tube model, Science and Technology Development Journal 18 (4) (2015) 153–161.
[36] M. Islam, D.S.-K. Ting, A. Fartaj, Aerodynamic models for darrieus-type straight-bladed vertical axis wind turbines, Renew. Sustain. Energy Rev. 12 (4) (2008) 1087–1109.
[37] M.R. Castelli, A. Englaro, E. Benini, The darrieus wind turbine: proposal for a new performance prediction model based on CFD, Energy 36 (8) (2011) 4919–4934.
[38] I. Paraschivoiu, Double-multiple streamtube model for darrieus wind turbines, NASA Wind Turbines Dynamics Workshop (1981) 19–25.
[39] Y. Li, S. Zhao, C. Qu, G. Tong, F. Feng, B. Zhao, T. Kotaro, Aerodynamic characteristics of straight-bladed vertical axis wind turbine with a curved-outline wind gathering device, Energy Convers. Manag. 203 (2020) 112249.
[40] I.C.M. Lositaño, L.A.M. Danao, Steady wind performance of a 5 kW three-bladed H-rotor darrieus vertical axis wind turbine (VAWT) with cambered tubercle leading edge (TLE) blades, Energy 175 (2019) 278–291.
[41] Y. Guo, X. Li, L. Sun, Y. Gao, Z. Gao, L. Chen, Aerodynamic analysis of a step adjustment method for blade pitch of a VAWT, J. Wind Eng. Ind. Aerod. 188 (2019) 90–101.
[42] S. Karimian, A. Abdolahifar, Performance investigation of a new darrieus vertical axis wind turbine, Energy 191 (2020) 116551.
[43] H. Lei, D. Zhou, Y. Bao, Y. Li, Z. Han, Three-dimensional improved delayed detached eddy simulation of a two-bladed vertical axis wind turbine, Energy Convers. Manag. 133 (2017) 235–248.
[44] S.B. Qamar, I. Janajreh, A comprehensive analysis of solidity for cambered darrieus VAWTs, Int. J. Hydrogen Energy 42 (30) (2017) 19420–19431.